This is a preprint of the following article, which is available from http://mdolab.engin.umich.edu
Gustavo L. O. Halila, Joaquim R. R. A. Martins, Krzysztof J. Fidkowski, Adjoint-Based Aerodynamic Shape Optimization Including Transition to Turbulence Effects. *Aerospace Science and Technology*, 2020.
The published article may differ from this preprint, and is available by following the DOI: https://doi.org/10.1016/j.ast.2020.106243.

Adjoint-Based Aerodynamic Shape Optimization Including Transition to Turbulence Effects

Gustavo L. O. Halila, Joaquim R. R. A. Martins, Krzysztof J. Fidkowski
Department of Aerospace Engineering, University of Michigan, Ann Arbor, MI, 48109

Abstract

The inclusion of transition to turbulence effects in aerodynamic shape optimization makes it possible to use it as a tool for the design of airframes with laminar flow. Modified Reynolds-Averaged Navier–Stokes (RANS) models that consider transition to turbulence have gained traction in the computational fluid dynamics (CFD) community. These models enable the computation of transitional flows without the need for external modules. In this work, we use a smooth version of the amplification factor transport (AFT) model, called AFT-S, to perform gradient-based aerodynamic shape optimization (ASO) of airfoils in subsonic and transonic flow conditions. We investigate the benefits of including transition effects into the optimization process and assess the impact of losing laminar flow when early transition to turbulence occurs due to surface contamination. Our results indicate that our design optimization approach yields lower drag airfoils when transition effects are considered. For the transonic case, the optimizer trades between shock wave strength and laminar flow extension to minimize drag.

1 Introduction

The inclusion of transition to turbulence effects in the aerodynamic design process is currently a major research area in the aerospace industry. The design of laminar flow airframes relies on the ability to predict transition to turbulence. It is expected that the use of laminar flow technologies, combined with turbulence and separation control techniques, will lead to a 15% total drag reduction for typical jetliners at cruise conditions [1].

Nonetheless, the importance of including transition to turbulence effects in daily computational fluid dynamics (CFD) simulations extends beyond laminar flow technology. There is evidence that considerable regions of laminar flow are present over the wings of a prototypical jet airplane configuration not designed to achieve laminar flow [2, 3]. This was observed for different flight conditions, with mean aerodynamic chord-based Reynolds numbers from 3 to 20 million and Mach numbers from 0.5 to 0.74. Therefore, including transition effects in CFD studies increases agreement with experimental data [2, 4].

The inclusion of transition effects into CFD simulations also benefits the analysis of high-lift configurations. In high-lift devices, each element experiences reduced Reynolds numbers, so that regions of laminar and transitional flow appear [5, 6]. Therefore, it is necessary to include a transition prediction capability to any computational tool used in high-lift design [4]. Computational results that include transition prediction in high-lift analysis through the use of an e^N method have demonstrated the importance of transitional effects in computational analysis of high-lift surfaces [7, 8]. Results in these papers indicated that an improved prediction capability, with good agreement with experimental data, is obtained when transition is included. More recently, numerical results showed that including transition to turbulence in the analysis of 3-D high-lift configurations improves correlation with experimental data when compared to fully-turbulent simulations [4].

Reynolds–Averaged Navier–Stokes (RANS) turbulence models, which are commonly used in engineering applications, are the result of a Favre time-averaging of the original Navier–Stokes equations. Modeling of transition to turbulence is performed through the inclusion of additional transport equations, generally supported by empirical correlations. Langtry and Menter [9–12] proposed a transition model where two additional transport equations are used to estimate transition onset and region extent. Transition onset is triggered by the momentum thickness Reynolds number (Re_θ) transport equation, and the intermittency (γ) transport equation is used to estimate the extent of the transition region. This model is coupled to the shear stress transport (SST) turbulence model [13].

A RANS transition model based on linear stability theory was proposed by Coder and Maughmer [14]. They proposed a transport equation for the approximate N-factor envelope, $\tilde{n}$, based on the work of Drela and Giles [15], with the Spalart–Allmaras [16] (SA) turbulence model as the base for the new two-equation transition model, called amplification factor transport (AFT). The AFT model was then augmented with an additional transport equation for the modified intermittency, $\tilde{\gamma}$, to improve its robustness when complex flows are considered [17]. The AFT model uses the notion of a local boundary layer shape factor, H_L, which is then mapped to the real shape factor, H_{12}. When compared with the original Langtry–Menter transition model, the AFT model has three transport equations, compared to four transport equations for the former. The AFT model was proposed as a tool to study external aerodynamic flows. However, the Langtry–Menter model was originally developed to investigate transitional flows in turbomachinery, where the turbulence levels are higher than those typically found in wind tunnels or in free flight.

At present, complex aircraft configurations are optimized considering high-fidelity,

RANS-based CFD calculations. As an example, Lyu et al. [18] were able to perform a lift-constrained drag minimization of the Common Research Model (CRM) wing with a RANS turbulence model. The corresponding wing-body-tail configuration was also optimized [19]. An aerostructural optimization has also been performed by Kenway and Martins [20], and a boundary layer ingestion propulsion system was investigated using adjoint-based optimization [21]. When performing gradient-based aerodynamic shape optimization (ASO), adjoint methods are the most efficient, since their computational cost is mostly independent of the number of design variables.

Adjoint methods were first used within the optimal control community, with the works of Lions [22] and Bryson and Ho [23]. Adjoint methods were then used to solve structural optimization problems [24, 25]. The use of the adjoint method in fluid mechanics was first introduced by Pironneau [26], who derived the adjoints of the Stokes equations and of the Euler equations [27]. In 1988, Jameson [28] extended the method to inviscid compressible flows, making it suitable for transonic airfoil design. The adjoint method was then applied to the Navier–Stokes equations by Jameson et al. [29] and by Nielsen and Anderson [30].

The inclusion of laminar turbulent transition in ASO computations is desirable because it enables the exploitation of laminar flow for drag minimization. However, the literature results considering high-fidelity aerodynamic shape optimization with transition to turbulence are sparse [31]. Dodbele [32] proposed an optimization method to design axisymmetric bodies with high transition Reynolds numbers in subsonic, compressible flow. The proposed approach used the Granville transition criterion [33] to compute the gradients of the objective function and an e^N method to compute the functional value at the end of each design iteration. The use of the Granville transition criterion to compute the gradients was motivated by its reduced computational cost when compared to the e^N method. Green et al. [34] proposed an approach to design airfoils with a large laminar flow region while satisfying geometric and aerodynamic constraints. Their approach is based on the prescription of a pressure distribution that stabilizes flow instabilities, and stability analysis was used to predict the transition location. Kroo and Sturdza [35] used a design-oriented aerodynamic analysis to perform direct optimization of supersonic wings employing laminar flow. They coupled a boundary layer solver with an Euler solver and a numerical optimization tool, and designed a wing with a minimum total drag at Mach 1.6.

Amoignon et al. [36] used a boundary layer solver coupled to a transition tool based on the parabolized stability equations (PSE) to delay transition based on an Euler solver. In their framework, the pressure coefficient distribution from an Euler solver is used as a boundary condition for a boundary layer solver. The boundary layer solver then provides the PSE code the boundary layer velocity profiles needed for the stability computation. In the reverse direction, their adjoint PSE code feeds the adjoint boundary layer code, which finally provides inputs to the adjoint Euler solver. They delayed transition by minimizing a measure of the disturbance kinetic energy of a chosen disturbance, which is computed using the PSE.

Driver and Zingg [37] used MSES [38], which is an Euler code augmented with boundary layer corrections, to predict transition location using an e^N approach. The predicted transition front was then used in a RANS solver that uses a Newton–Krylov

discrete-adjoint optimization algorithm. Their algorithm was then used to design airfoils with maximum lift-to-drag ratio, endurance factor, and lift coefficient. In that work, the transition prediction module was loosely coupled to the RANS solver.

Lee and Jameson [39, 40] coupled a transition module based on two e^N-database methods considering Tollmien–Schlichting (TS) waves and crossflow vortices with a flow solver to predict and prescribe transition locations automatically. This study showed that natural laminar flow optimized airfoil and wings not only presented improvements in the single design point, but also performed well in off-design conditions. Their flow solver used the Baldwin–Lomax turbulence model [41], an algebraic, 0-equation model. They used a computational approach that creates turbulent patches starting at the transition location specified by the transition module. Because of this, the blending between laminar and turbulent regions was not smooth. Additionally, the gradient computations used in their work did not consider the transition prediction itself.

Khayatzadeh and Nadarajah [42, 43] used the γ-$\tilde{Re}_\theta$ model [9] to perform aerodynamic shape optimization of natural laminar flow airfoils. This model is also commonly referred to as the Langtry–Menter transition model. They applied their framework to the design of low Reynolds NLF airfoils that exhibit separation bubbles. They also showed that, for subsonic flows where viscous drag dominates, turbulent kinetic energy can be an alternative to total drag as an objective function.

Recent research results [44–46] have used the Langtry–Menter model to perform finite-difference gradient-based aerodynamic optimization, which represents a costly approach. Rashad and Zingg [31] used a 2-D RANS solver coupled to a simplified e^N method or to the Arnal–Habiballah–Delcourt criterion [47] in a discrete adjoint capability to perform airfoil natural laminar flow optimization. A simplified e^N method was used to perform adjoint-based airfoil aerodynamic shape optimization with transition effects in a recent work [48].

In this work, we use a smooth variant of the original AFT model, referred to as AFT-S, to perform aerodynamic shape optimization. We propose a RANS-based, self-contained aerodynamic shape optimization framework that is able to consider transition to turbulence effects. This framework is unique in that it does not resort to external modules to include transition in the CFD computations, uses gradient-based optimization in which the transition transport equations are part of the adjoint formulation, and considers the flow stability-based AFT-S model. We perform aerodynamic shape optimization of airfoils with flight conditions ranging from subsonic to transonic regimes. These simulations include fully-turbulent and transitional cases. We demonstrated the benefits of including transition in the optimization process by comparing the results. We investigate the effects of early transition caused by flow contamination by running the natural laminar flow airfoils in fully-turbulent mode and show that airfoils optimized while considering transition exhibit similar performance to airfoils optimized without considering transition when the flow conditions make it impossible to achieve significant laminar flow.

The rest of the paper is organized as follows. In Sec. 2, we introduce the AFT model. We present our aerodynamic shape optimization framework in Sec. 3 Aerodynamic shape optimization results for transitional and turbulent flows are shown in Sec. 4. We

conclude this paper with final remarks in Sec. 5.

2 Amplification Factor Transport Transition Model

The Amplification Factor Transport (AFT) model was first proposed by Coder and Maughmer [14]. The original model was modified so that no isentropic flow assumption was needed and that Galilean invariance was achieved [49]. In a next version, the transport equation for the modified intermittency, $\tilde{\gamma} = \ln(\gamma)$, was introduced to improve robustness when complex flows are considered [50]. A modified intermittency function was used so that the model could be implemented with different solver strategies, including finite-element methods. Finally, after modifying some of the correlations that feed the transport equations, a new version was released [17]. In the current AFT model implementation, the transport equations model the amplification of three-dimensional TS waves, but crossflow (CF) modes are not considered. Carnes and Coder [51] recently proposed the use of empirical correlations initially introduced by Langtry [52] to include stationary CF effects into the AFT model. In the AFT model, the inflow perturbations amplitudes are indirectly included in the modeling strategy through the turbulence intensity, T_u. Differently from other RANS transition models, the AFT model makes possible a direct correlation between experimental T_u levels and the inflow conditions used with the model. Since the AFT model is based on an e^N analysis, nonlinear effects that precede breakdown to turbulence are not part of the modeling strategy. For typical airplane configurations, the use of linear flow stability techniques to predict the transition onset location has proved accurate from an engineering perspective [53, 54].

The approximate N-factor, $\tilde{n}$, is transported following the relation

$$\frac{\partial(\rho\tilde{n})}{\partial t} + \frac{\partial(\rho u_j \tilde{n})}{\partial x_j} = \rho\Omega F_{\text{growth}} F_{\text{crit}} \frac{d\tilde{n}}{dRe_\theta} + \frac{\partial}{\partial x_j}\left[\sigma_n \left(\mu + \mu_t\right) \frac{\partial \tilde{n}}{\partial x_j}\right], \tag{1}$$

where ρ is the density, Ω is the vorticity magnitude, μ is the molecular dynamic viscosity, μ_t represents the eddy viscosity, and $\sigma_n = 1$ is a model constant.

The intermittency, γ, is the probability of a given point in the flow field being turbulent. A unit value represents fully-turbulent flow and a zero value corresponds to a laminar state. The modified intermittency, $\tilde{\gamma}$, relates to the intermittency through the mapping $\tilde{\gamma} = \ln(\gamma)$. The transport equation for the approximate intermittency is given by

$$\begin{aligned}\frac{\partial(\rho\tilde{\gamma})}{\partial t} + \frac{\partial(\rho u_j \tilde{\gamma})}{\partial x_j} = {} & c_1 \rho S F_{\text{onset}} \left[1 - \exp(\tilde{\gamma})\right] - c_2 \rho \Omega F_{\text{turb}} \left[c_3 \exp(\tilde{\gamma}) - 1\right] \\ & + \frac{\partial}{\partial x_j}\left[\left(\mu + \frac{\mu_t}{\sigma_\gamma}\right) \frac{\partial \tilde{\gamma}}{\partial x_j}\right],\end{aligned} \tag{2}$$

where the model constants are $c_1 = 100$, $c_2 = 0.06$, $c_3 = 50$, and $\sigma_\gamma = 1.0$. For TS waves, the original Mack correlation [55] can be used,

$$N_{\text{crit,TS}} = -8.43 - 2.4 \ln\left(\frac{\tau}{100}\right), \tag{3}$$

where the variable τ relates to the real percentage turbulence intensity, T_u, according to

$$\tau = 2.5\tanh\left(\frac{T_u}{2.5}\right). \tag{4}$$

Here, τ is defined to only allow positive values for N_{crit}. The critical N-factor is then used in onset functions that feed the source terms in the modified intermittency transport equation. Coder [17] provides more details on the functions that are part of the model.

The boundary conditions for both AFT working variables are homogeneous Dirichlet in the freestream and homogeneous Neumann on solid walls:

$$\tilde{n}_\infty = \tilde{\gamma}_\infty = 0, \tag{5}$$

$$\left.\frac{\partial \tilde{n}}{\partial y}\right|_\infty = \left.\frac{\partial \tilde{\gamma}}{\partial y}\right|_\infty = 0. \tag{6}$$

Again, Coder [17, 50] provides more details on the standard AFT transition model.

The underlying SA turbulence model is given by,

$$\begin{aligned}\frac{D\tilde{\nu}}{Dt} = {} & c_{b1}S\tilde{\nu}\left(1 - f_{t2}\right) - \left(c_{w1}f_w - \frac{c_{b1}}{\kappa^2}f_{t2}\right)\left(\frac{\tilde{\nu}}{d}\right)^2 \\ & + \frac{1}{\sigma}\left\{\frac{\partial}{\partial x_j}\left[(\nu + \tilde{\nu})\frac{\partial \tilde{\nu}}{\partial x_j}\right] + c_{b2}\frac{\partial \tilde{\nu}}{\partial x_j}\frac{\partial \tilde{\nu}}{\partial x_j}\right\},\end{aligned} \tag{7}$$

and the coupling between the transition and turbulence transport equations takes place through a modification in the original f_{t2} function, that becomes

$$f_{t2} = c_{t3}\left[1 - \exp(\tilde{\gamma})\right]. \tag{8}$$

The relation between the SA working variable, $\tilde{\nu}$, and the eddy viscosity, μ_t, is,

$$\mu_t = \rho\tilde{\nu}\frac{\chi^3}{\chi^3 + c_{v1}^3}, \tag{9}$$

where

$$\chi = \frac{\tilde{\nu}}{\nu}. \tag{10}$$

Allmaras and Johnson [56] describe the other variables in Eqs. (7) to (10) in more detail.

We modify the original AFT model, which has minimum and maximum functions, as well as switching step functions that are discontinuous, to make the model smooth and thus compatible with gradient-based optimization. We call the smooth variant AFT-S. More details on our smoothing strategy can be found in Ref. [57]. We also used a similar smoothing approach to perform aerodynamic shape optimization with a simplified e^N method [48].

The step function is used in the F_{crit} step function, as described by Coder [17]. We smooth this step function by using a modified hyperbolic tangent. The resulting function is,

$$F_{\text{crit}} = \frac{1}{2}\left[1 + \tanh\left(\frac{Re_v - Re_{v,0}}{f_{\text{smooth}}}\right)\right], \tag{11}$$

where f_{smooth} is a constant set to 300 in the current implementation.

The minimum and maximum functions are made smooth by using the Kreisselmeier–Steinhauser (KS) function [58], which has been used for constraint aggregation in structural optimization [59, 60]. The maximum of functions F_1 and F_2 in a given computational cell is computed using a KS function as follows,

$$\max\left(F_1, F_2\right) = \frac{\ln\left[\exp\left(p_{\max}F_1\right) + \exp\left(p_{\max}F_2\right)\right]}{p_{\max}}, \tag{12}$$

where ln is the natural logarithm and $p_{\max}$ is a positive constant set to 100 in the current implementation. Equivalently, the minimum of functions F_1 and F_2 is computed by,

$$\min\left(F_1, F_2\right) = \frac{\ln\left[\exp\left(p_{\min}F_1\right) + \exp\left(p_{\min}F_2\right)\right]}{p_{\min}}, \tag{13}$$

where $p_{\min}$ is a negative constant, chosen to be -100 in our current implementation. We have presented a study on the AFT-S model validation against experimental data in Ref [57]. As an example, the results in Fig. 1, reproduced from our previous work [57], illustrate the transition front location and drag polar for a NLF(1)-0416 airfoil at $Re = 4 \times 10^6$ and $M = 0.1$. For these validation results, a freestream turbulence intensity of $Tu = 0.15\%$ was used.

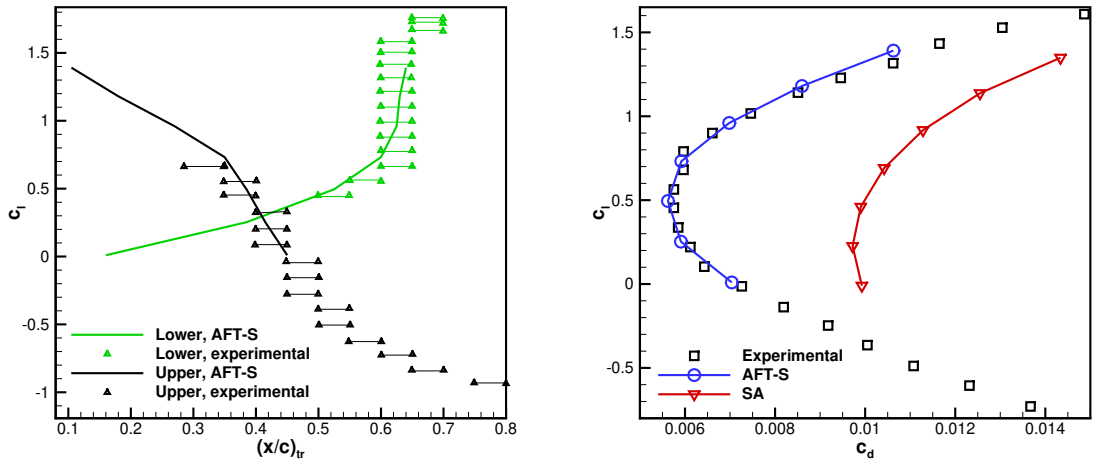

(a) Transition locations

(b) Drag polar

Figure 1: Transition locations (left) and drag polar (right) for angles of attack from -8 to 4 degrees [57].

3 Aerodynamic Shape Optimization Framework

Our aerodynamic shape optimization (ASO) framework uses ADflow as the flow solver. ADflow is an open source, in-house developed CFD solver [61]. ADflow has options to solve Euler, laminar Navier–Stokes, and RANS equations in steady, unsteady, and time-spectral modes, with multiblock structured and overset meshes. The inviscid fluxes are

discretized by using three different numerical schemes: the scalar Jameson–Schmidt–Turkel [62] (JST) artificial dissipation scheme, a matrix dissipation scheme based on the work of Turkel and Vatsa [63], and a monotone upstream-centered scheme for conservation laws (MUSCL) based on the work of van Leer [64] and Roe [65]. The viscous flux gradients are calculated by using the Green–Gauss approach. The residual equations can be converged with four distinct algorithms. Runge–Kutta and diagonalized-diagonally-dominant alternating direction implicit [66] (D3ADI) algorithms are available. An approximate Newton–Krylov (ANK) solver is also implemented and can be used as a globalization scheme for the full Newton-Krylov algorithm [67]. Due to its robustness and numerical behavior, we adopt the ANK solver in this work. ADflow also includes an adjoint solver [68], and is part of a framework that has been successfully used for aerodynamic shape optimization [18, 69–72].

The design variable vector, $\mathbf{x}$, contains both aerodynamic and geometric design variables. While derivatives of the objective function with respect to aerodynamic design variables are computed directly, we use a chain rule to calculate derivatives with respect to geometric design variables. This is,

$$\frac{d\mathbf{f}}{d\mathbf{x}} = \frac{d\mathbf{f}}{d\mathbf{x}_\mathrm{v}} \frac{d\mathbf{x}_\mathrm{v}}{d\mathbf{x}_\mathrm{s}} \frac{d\mathbf{x}_\mathrm{s}}{d\mathbf{x}}, \tag{14}$$

where subscripts v and s indicate the volume and the design surface coordinates, respectively. We compute the derivatives $d\mathbf{x}_\mathrm{s}/d\mathbf{x}$ and $d\mathbf{x}_\mathrm{v}/d\mathbf{x}_\mathrm{s}$ by using two external open-source geometry modules, pyGeo [73] and IDWarp [74]. In pyGeo, the geometry is parametrized using the free-form deformation (FFD) technique [75]. The FFD is a mapping of a region in 2-D or 3-D that is bounded by a set of B-splines. The B-splines are defined by a set of control points that constitute the shape design variables. As we perform constrained optimization, we also compute the geometric constraint derivatives. In IDwarp, an efficient analytic inverse-distance method is used [74, 76]. The derivative $d\mathbf{f}/d\mathbf{x}_\mathrm{v}$ is computed in ADflow. By doing this, we assure that the adjoint implementation does not depend on external geometric parametrization and mesh deformation modules [77, 78]. Kenway et al. [68] provide a detailed description of the adjoint derivative computation used in ADflow.

In this work, we use the SNOPT general-purpose sequential quadratic programming algorithm as the optimizer [79]. This optimizer is suitable for solving large-scale nonlinear optimization problems. We use the open-source package pyOptSparse [80], which wraps SNOPT.

The CFD-based aerodynamic shape optimization framework described above has been used to perform several investigations [69, 70, 81–85]. Martins [86] provides a summary of these investigations.

4 Aerodynamic Shape Optimization with Transition to Turbulence Effects

Our objective is to reduce drag rather than delaying transition, even though these are correlated objectives in subsonic flow. For subsonic flows with minor separation

regions, drag is dominated by skin friction effects. Therefore, transition delay leads to drag reduction. In transonic cases, the wave drag is relevant and should be considered in the optimization process [45]. This suggests a compromise between the extent of the laminar region and shock wave strength, since extended laminar regions usually require pressure distributions that increase the latter, raising the total drag. Therefore, we focus on lift-constrained drag minimization in this work. The design variables are shape variables and angle of attack.

For the airfoil optimization problems discussed here, we impose area and thickness constraints. To prevent the shape variables from creating a shearing twist, we enforce the upper and lower nodes on the leading and trailing edges to move in opposite directions. The optimization problem is defined in Table 1.

Table 1: Optimization problem formulation for the airfoil cases. The objective is to minimize drag.

	Function/variable	Description	Quantity
minimize c_d			
with respect to	x_{shape}	Shape design variables	6
	α	Angle of attack	1
subject to	$c_l = c_l^*$	Lift constraint	1
	$0.9(t/c)_{\text{base}} \leq (t/c)$	Thickness constraint	1
	$0.93V_{\text{base}} \leq V \leq 1.07V_{\text{base}}$	Area constraint	1

4.1 NACA 0012

We select the NACA 0012 airfoil as our first aerodynamic shape optimization (ASO) case. The optimization is run on 36 processors for up to 72 hours. Intel Xeon Gold 6154 processors are used in this simulation, running at 3.0 GHz with 5 GB of RAM per processor. The flight condition is $Re = 4 \times 10^6$ at $M = 0.2$. The reference temperature is $T = 300.0$K. The molecular dynamic viscosity is computed using Sutherland's law for all simulations in this paper. To reproduce a low-turbulence environment, we use a freestream turbulence intensity of $Tu = 0.15\%$, corresponding to $N_{\text{crit}} = 7.17$, according to Eq. (3).

Fully-turbulent and transitional aerodynamic shape optimizations are performed, using the SA and AFT-S models, respectively. The target lift coefficient is $c_l = 0.3$.The leading and trailing edge geometries are preserved using linear constraints, and the thickness is not allowed to reduce below 10% of the original value. The airfoil section area is constrained such that it does not vary by more than 7% relative to the original area. For the airfoil cases depicted in this work, we use an FFD with 8 design variables. The two control points placed in the leading edge region move together to preserve the shape in this location and, therefore, represent a single design variable. The same holds for the trailing edge, leading to 6 effective shape design variables. The airfoil incidence, seen here as the angle of attack, is also used as a design variable. The transitional ASO starts with an angle of attack of 2.19 degrees, with a 1.50-degree angle of attack in the

optimized configuration. For the turbulent ASO, the optimized design is at an angle of attack of 1.17 degrees.

The airfoil resulting from the transitional ASO resembles the natural laminar flow NACA 66(1)-212 airfoil, which has a lift coefficient value of $c_l = 0.3$ in the center of the laminar bucket region [87]. For both fully-turbulent and transitional optimized shapes, the baseline airfoil symmetry is lost. This is consistent with the fact that a nonzero value is targeted for the lift coefficient. Baseline and optimized airfoils are illustrated in Fig. 2. The baseline NACA 0012 airfoil corresponds to the black shape. The optimized airfoil resulting from flow simulations using the AFT-S model is shown in blue, and the fully-turbulent optimization using the SA model is depicted in red in the zoom-in figure.

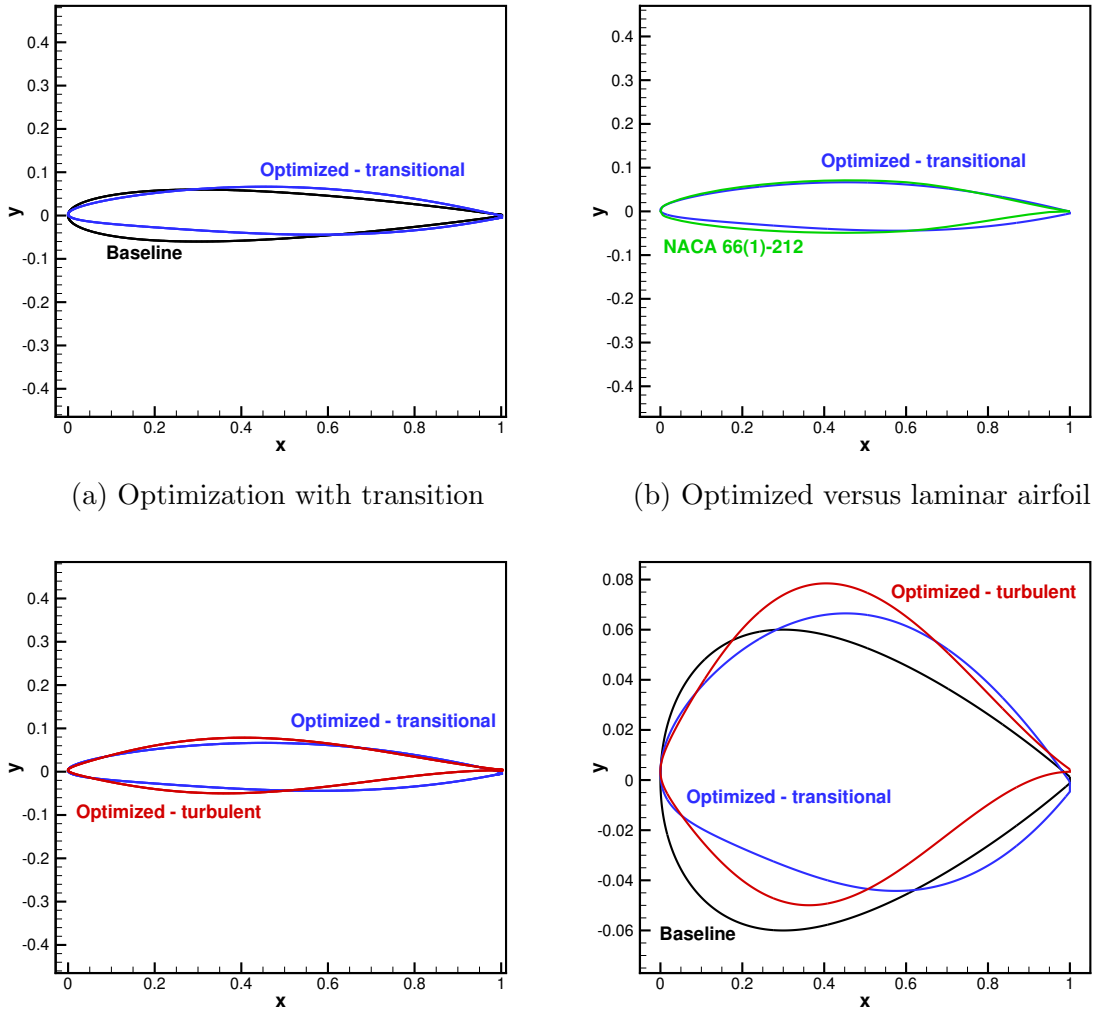

(a) Optimization with transition

(b) Optimized versus laminar airfoil

(c) Comparison with turbulent optimization

(d) Zoomed-in y-axis.

Figure 2: Baseline and optimized airfoils.

The fully-turbulent ASO results in an airfoil with a 3.29% drag reduction compared with the baseline, fully-turbulent case. When transition is included using the

AFT-S model, the optimized airfoil exhibits a drag 33.20% smaller than the baseline case including transition to turbulence. The optimizer explores the design space more effectively when more physics are included in the CFD solution, and the drag benefit is noticeable. The aerodynamic drag coefficients for both ASO cases are listed in Table 2.

Table 2: Drag reduction for the NACA 0012 airfoil. The target lift coefficient is $c_l = 0.3$.

Case	Baseline c_d	Optimized c_d	Drag difference (%)	Optimized c_l
Turbulent	0.00911	0.00881	3.29	0.2999
Transitional - NLF	0.00512	0.00342	33.20	0.2997

It is important to consider how early transition to turbulence affects the natural laminar flow airfoil performance. To address this, we perform a fully-turbulent simulation in the airfoil optimized with transition to turbulent effects, in what we call natural laminar flow airfoil in fully-turbulent mode. The simulations considering natural laminar flow airfoils in fully-turbulent mode are performed at the design c_l for all comparisons presented in this work. The resulting drag coefficient is $c_d = 0.00907$, which is 2.95% higher than the drag resulting from the fully-turbulent ASO. These numbers are summarized in Table 3. This indicates that an airfoil optimized with transition to turbulence included has a shape that retains good drag characteristics if in-flight contamination occurs. This aspect is related to the certification of laminar flow aircraft. The figures above consider a natural laminar flow airfoil operating with all surface in turbulent flow, which is an extreme scenario and, hence, characterizes a procedure used along with certification processes. In some cases, the effect of surface contamination may lead to premature transition in only some regions of the wing rather than an entirely turbulent flow field.

Table 3: Drag coefficients for the NACA 0012 airfoil cases considering turbulent optimization, transitional optimization, and natural laminar flow airfoil in fully-turbulent mode.

Case	c_d
Turbulent	0.00881
Transitional - NLF	0.00342
NLF airfoil in fully-turbulent mode	0.00907

In this subsonic drag minimization ASO, the optimizer exploits the possibility of moving the transition location on both airfoil sides. The transition front is delayed from $(x/c)_{\text{tr,baseline}} = 0.31$ to $(x/c)_{\text{tr,optimized}} = 0.66$ for the airfoil suction side, and from $(x/c)_{\text{tr,baseline}} = 0.72$ to $(x/c)_{\text{tr,optimized}} = 0.90$ in the airfoil pressure side. Skin friction and pressure coefficient distributions for the baseline and transitional ASO cases are shown in Fig. 3. The pressure coefficient contours in Fig. 3 indicate that the optimizer leads to a geometry that reduces the adverse pressure gradient in the upper airfoil side. By doing so, the TS wave amplification is delayed, moving the transition front

downstream, as observed above. Inspection of Fig. 3a indicates that some transitional flow features commonly observed in experimental and direct numerical simulation c_f plots are not present in the AFT predictions. For example, one can observe an abrupt skin friction coefficient change in the laminar to turbulent region. This is because, like other RANS models that consider transition effects, the AFT model does not attempt to directly model the transition region. Instead, the modified intermittency transport equation attempts to turn on the SA model source terms gradually, and therefore should be seen as an artifact to obtain a smooth transition zone rather than a true transition region model.

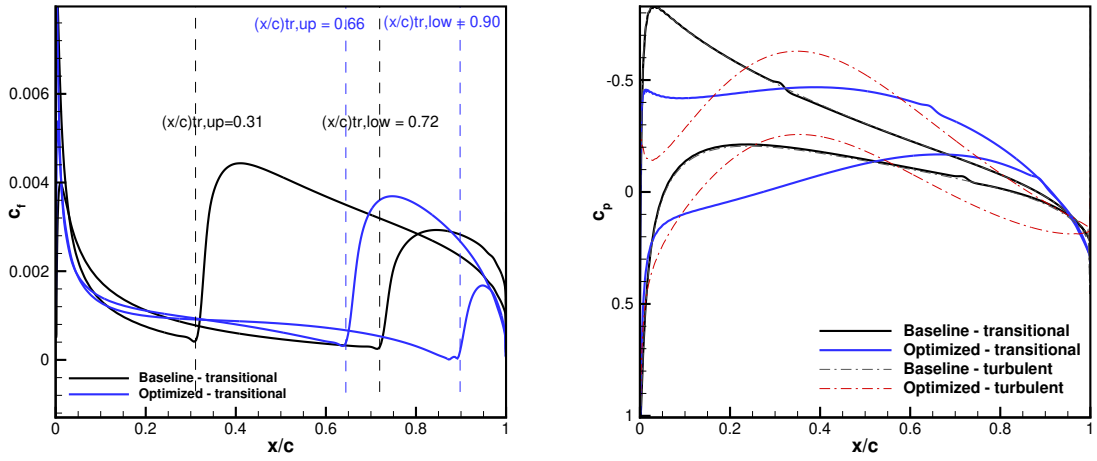

(a) c_f (b) c_p

Figure 3: Skin friction (left) and pressure (right) coefficients for the transitional ASO. Target lift coefficient $c_l = 0.3$.

The contours of the SA model working variable, $\tilde{\nu}$, further highlight the non-symmetric geometry in the optimized case and indicate a reduced turbulent region in the optimized geometry. These contours for transitional baseline and optimized shapes are shown in Fig. 4. In the AFT model, $\tilde{\gamma}$ tends to zero in fully-turbulent flow regions. The modified intermittency, $\tilde{\gamma}$, is initialized to zero values in the farfield, and a viscous wall damps turbulence effects in regions that are supposed to be laminar. In Fig. 5, we can see that the optimized shape exhibits turbulent $\tilde{\gamma}$ contours (yellow) entering the boundary layer region in a downstream position when compared to the baseline geometry.

As previously mentioned, in subsonic flow conditions, transition onset delay results in reduced drag because the drag coefficient is dominated by viscous effects. This physical behavior is observed in this NACA 0012 example.

We also perform multipoint aerodynamic shape optimization for transitional and fully-turbulent cases. The optimization is run on 36 processors for up to 72 hours. Intel Xeon Gold 6154 processors are used in this simulation, running at 3.0 GHz with 5 GB or RAM per processor. We select $Re = 4 \times 10^6$ and $M = 0.2$ and two distinct lift coefficients: $c_l = 0.3$ and $c_l = 0.5$. Both flight conditions are equally weighted.

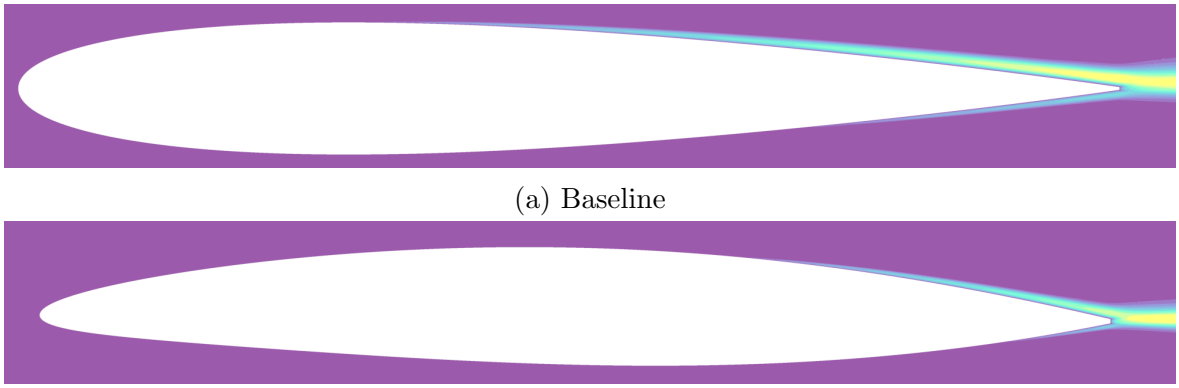

(a) Baseline

(b) Optimized

Figure 4: Contours of the SA model working variable, $\tilde{\nu}$, for the baseline geometry with transition included (top) and the optimized one (bottom). The contour range is from 1×10^{-6} to 9×10^{-6}. Target lift coefficient $c_l = 0.3$.

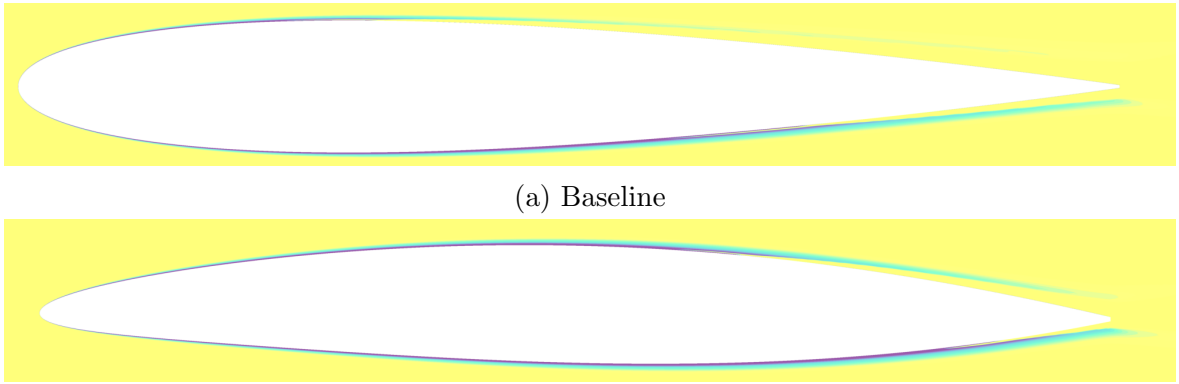

(a) Baseline

(b) Optimized

Figure 5: Contours of modified intermittency, $\tilde{\gamma}$, for the baseline geometry with transition included (top) and the optimized one (bottom). The contour range is from -3.8 (purple) to -0.2 (yellow). Target lift coefficient $c_l = 0.3$.

The reference temperature is $T = 300.0$K. We refer to the $c_l = 0.3$ point as flight condition 1, with $c_l = 0.5$ corresponding to flight condition 2. The resulting transition-based optimized airfoil retains some geometric features observed in the single-point optimization with $c_l = 0.3$. This is most noticeable in the airfoil pressure side. On the upper surface, the multipoint optimization including transition leads to an airfoil with more curvature, which accommodates the second flight condition lift coefficient, $c_l = 0.5$. The baseline, transitional, and turbulent ASO airfoils are illustrated in Fig. 6.

For the first flight condition, the fully-turbulent ASO case results in an airfoil with a 2.74% drag reduction compared with the baseline, fully-turbulent case. When transition is included using the AFT-S model, the optimized airfoil has a drag 26.17% smaller than the baseline case including transition to turbulence. For the second flight condition, the fully-turbulent ASO leads to a 3.72% drag reduction, while the transitional optimization results in an airfoil with a drag that is 31.14% smaller than the one

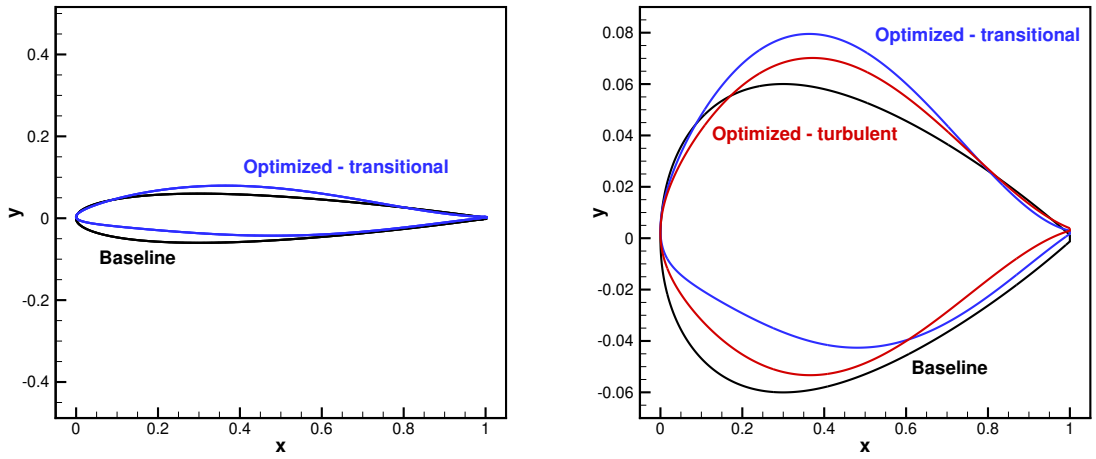

(a) Optimization with transition (b) zoom-in

Figure 6: Baseline and optimized airfoils. Multipoint case.

corresponding to the baseline airfoil in transitional mode. The aerodynamic coefficient information for the multipoint ASO is available in Table 4.

Table 4: Drag reduction for the NACA 0012 airfoil

Cond.	Case	Baseline c_d	Optimized c_d	Drag diff. (%)	Optimized c_l
1	Turbulent	0.00911	0.00886	2.74	0.2998
1	Transitional - NLF	0.00512	0.00378	26.17	0.2999
2	Turbulent	0.00967	0.00931	3.72	0.4997
2	Transitional - NLF	0.00607	0.00418	31.14	0.4999

If surface contamination leads to fully turbulent flow, the drag coefficient rises to 0.00895 for flight condition 1. This is 1.01% higher than the drag coefficient achieved in the fully-turbulent ASO in this condition, as well as in a multipoint study. For flight condition 2, the natural laminar flow airfoil in fully-turbulent mode leads to a drag coefficient of 0.00940, representing a 0.97% increase when compared to its fully-turbulent optimized counterpart. The numbers are shown in Table 5.

The single-point optimization for $c_l = 0.3$ resulted in an optimized airfoil with a drag coefficient of 34.2 drag counts. At this condition, the multipoint optimization leads to an airfoil that has a drag coefficient of 37.8 drag counts, representing an increase of 10.53% compared to the corresponding single-point ASO.

For flight condition 1, transition is delayed from $(x/c)_{\text{tr,baseline}} = 0.31$ to $(x/c)_{\text{tr,optimized}} = 0.50$ for the airfoil suction side. In the corresponding single-point ASO, transition was further delayed to $(x/c)_{\text{tr,optimized}} = 0.66$. For this same flight condition, the transition front was moved from $(x/c)_{\text{tr,baseline}} = 0.72$ to $(x/c)_{\text{tr,optimized}} = 0.83$ in the airfoil pressure side. In the single-point optimization at the same flight condition, the transition location was $(x/c)_{\text{tr,optimized}} = 0.90$. In flight condition 2, we see a transition delay

Table 5: Drag coefficients for the multipoint NACA 0012 airfoil cases considering turbulent optimization, transitional optimization, and natural laminar flow airfoil in fully-turbulent mode.

Cond.	Case	c_d
1	Turbulent	0.00886
1	Transitional - NLF	0.00378
1	NLF airfoil in fully-turbulent mode	0.00895
2	Turbulent	0.00931
2	Transitional - NLF	0.00418
2	NLF airfoil in fully-turbulent mode	0.00940

from $(x/c)_{\text{tr,baseline}} = 0.13$ to $(x/c)_{\text{tr,optimized}} = 0.44$ in the airfoil suction side. For flight condition 2, the transition location is basically unaltered in the pressure side, moving from $(x/c)_{\text{tr,baseline}} = 0.88$ to $(x/c)_{\text{tr,optimized}} = 0.87$. The skin friction coefficient distributions for the multipoint ASO are illustrated for both flight conditions in Fig. 7. The skin friction coefficient distribution for the natural laminar flow airfoil in fully-turbulent mode is also plotted in Fig. 7. As expected, the skin friction coefficient distribution is representative of fully-turbulent flow in this case. The large c_f values in the first half of the chord are responsible for the drag rise observed when laminarity is lost.

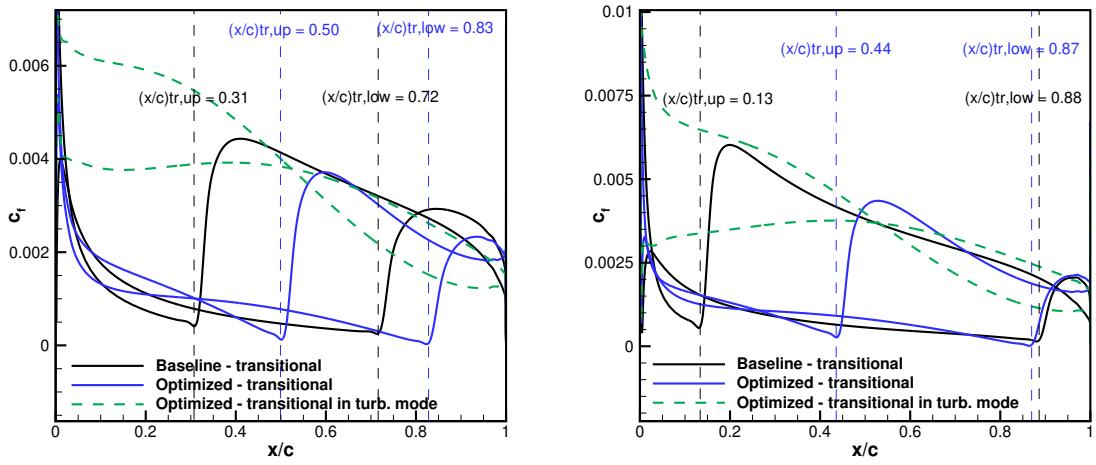

(a) $c_l = 0.3$ (b) $c_l = 0.5$

Figure 7: Skin friction coefficient for the transitional multipoint ASO case.

In flight condition 1, the airfoil obtained in the multipoint ASO including transition effects exhibits an extended favorable pressure gradient region on the suction side. This stabilizes TS waves, thereby delaying transition. When at flight condition 2, the airfoil resulting from the multipoint, transitional ASO exhibits a suction peak close to the leading edge. An adverse pressure gradient that is more pronounced than the one

corresponding to the single-point case ($c_l = 0.3$) follows, but does not trigger transition to turbulence. Starting at 6.5% of the chord, a new favorable pressure gradient develops, and transition eventually takes place at 44% of the chord. For the same flight condition, the fully-turbulent multipoint ASO leads to an airfoil that exhibits a more pronounced adverse pressure gradient in the leading edge region. In the transitional case, the optimizer exploits the additional physics and provides a design that avoids premature transition at the leading edge by minimizing the adverse pressure gradient in that region. The pressure coefficient distributions for the multipoint ASO studies are shown in Fig. 8. Pressure coefficient distributions for the natural laminar flow airfoil in fully-turbulent mode are also shown in Fig. 8. Since the same lift coefficient as in the transitional case is maintained in the natural laminar flow airfoil in fully-turbulent mode simulations, the pressure coefficient distributions are close to the ones corresponding to the optimized airfoil in transitional mode. Some small differences are observed, however, in the regions where transition takes place in the transitional simulation.

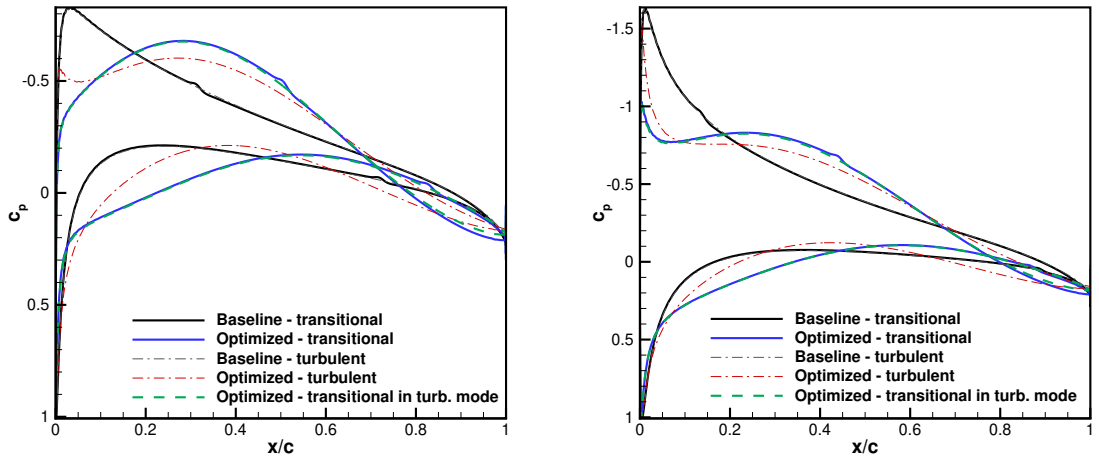

(a) $c_l = 0.3$ (b) $c_l = 0.5$

Figure 8: Pressure coefficient for the transitional multipoint ASO case.

For the airfoil resulting from the transitional multipoint ASO, the increase in angle of attack needed to increase the lift coefficient from $c_l = 0.3$ to $c_l = 0.5$ leads to an upstream movement of the transition point, from 50% to 44% of the chord. This effect can be seen by comparing the modified intermittency, $\tilde{\gamma}$, for the optimized airfoil when in both flight conditions considered in the multipoint ASO. The increase in angle of attack, from 2.19 to 3.89 degrees, increases the adverse pressure coefficient on the suction side. This destabilizes TS waves, which are amplified under adverse pressure gradient conditions. As a consequence, the modified intermittency contours indicate that the turbulent region, corresponding to $\tilde{\gamma}$ approaching zero, develops upstream in the higher lift coefficient flight condition. Modified intermittency contours for the transitional multipoint airfoil in both flight conditions are shown in Fig. 9.

When natural laminar flow airfoils are designed, it is relevant to investigate the

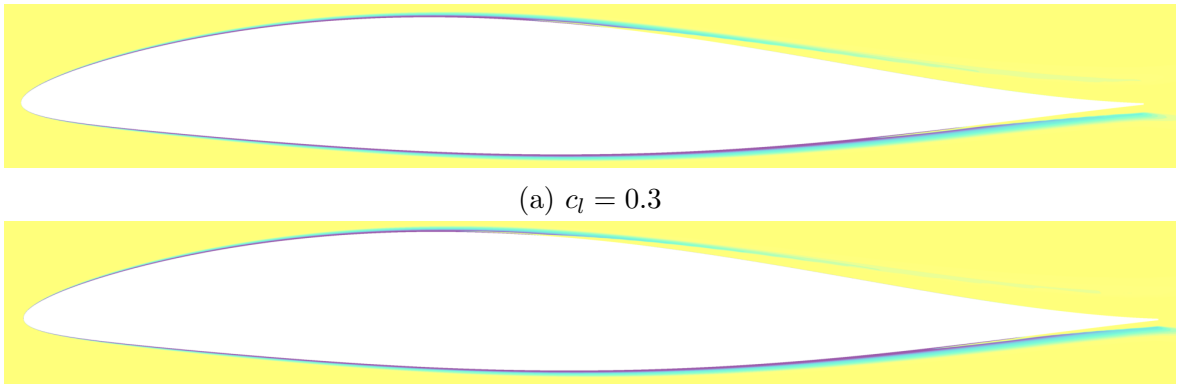

(a) $c_l = 0.3$

(b) $c_l = 0.5$

Figure 9: Contours of modified intermittency, $\tilde{\gamma}$, for the multipoint optimization with transition included. The contour range is from -3.8 (purple) to -0.2 (yellow).

behavior at high angles of attack. Laminar boundary layers are more prone to separation than turbulent ones. Therefore, the maximum lift at these high angles of attack depend on the characteristics of the turbulent boundary layer and its ability to recover pressure at the rear of the airfoil [88]. Future investigations will include the high angle of attack behavior as part of the optimization process considering transitional flows.

4.2 RAE 2822

We perform aerodynamic shape optimization for the RAE 2822 transonic airfoil in transitional and fully-turbulent modes. The optimization is run on 192 processors for up to 72 hours. Intel Xeon Platinum 8160 processors are used in this simulation, running at 2.1 GHz with 4 GB of RAM per processor. We select a flight condition defined by a Mach number of 0.729 and a Reynolds number of 6.5×10^6. The reference temperature is $T = 273.15$K. The optimization settings used for the RAE 2822 case are the same as the ones used for the NACA 0012 airfoil. For the transitional cases with the AFT-S model, we select a freestream turbulence intensity of $Tu = 0.15\%$, corresponding to $N_{\text{crit}} = 7.17$ according to Eq. (3). The target lift coefficient is $c_l = 0.74$. The leading and trailing edge geometries are preserved using linear constraints, and the thickness is not allowed to reduce below 10% of the original value. The airfoil section area is constrained such that it does not vary by more than 7% relative to the original area. The transitional ASO starts with an angle of attack of 2.25 degrees, with a 2.29-degree angle of attack in the optimized configuration. For the turbulent ASO, the initial angle of attack is of 2.31 degrees, and the optimized design is at an angle of attack of 2.47 degrees.

The baseline and optimized airfoils are shown in Fig. 10. The baseline RAE 2822 airfoil corresponds to the black shape. The optimized airfoil resulting from flow simulations using the AFT-S model is shown in blue, and the fully-turbulent optimization using the SA model is shown in red in Fig. 10b.

The fully-turbulent ASO leads to a reduction of 20.06% in the drag coefficient, with a baseline value of 123.1 drag counts and an optimized drag coefficient of 98.4

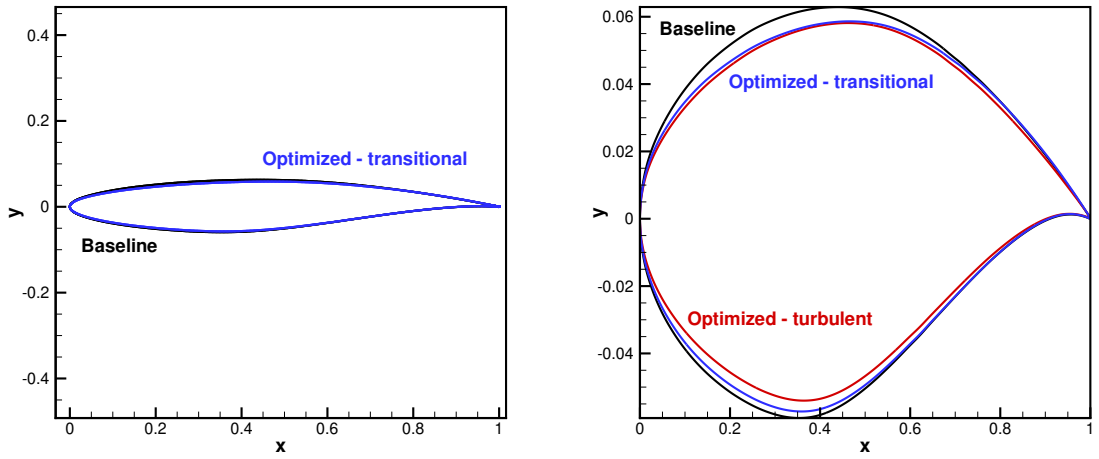

(a) Optimization with transition

(b) Zoomed-in y-axis.

Figure 10: Baseline and optimized airfoils for RAE 2822 case.

drag counts. The transitional optimization yields a 28.081% drag reduction, with a baseline drag coefficient of 108.6 drag counts that is reduced to 78.1 drag counts in the optimal design. If the transitional-optimized airfoil loses laminar flow because of surface contamination or another reason, the resulting fully-turbulent drag coefficient is 99.52 drag counts, which is 1.13% higher than the drag corresponding to the airfoil obtained in the fully-turbulent ASO. The aerodynamic drag coefficients for both ASO cases are presented in Table 6, while the numbers for the natural laminar flow airfoil in fully-turbulent mode are shown in Table 7.

Table 6: Drag reduction for the RAE 2822 airfoil

Case	Baseline c_d	Optimized c_d	Drag difference (%)	Optimized c_l
Turbulent	0.001231	0.00984	20.06	0.7397
Transitional - NLF	0.001086	0.00781	28.08	0.7430

Table 7: Drag coefficients for the RAE 2822 airfoil cases considering turbulent optimization, transitional optimization, and natural laminar flow airfoil in fully-turbulent mode.

Case	c_d
Turbulent	0.00984
Transitional - NLF	0.00781
NLF airfoil in fully-turbulent mode	0.00995

In the transitional ASO, the transition front location is moved from $(x/c)_{\text{tr,baseline}} = 0.105$ to $(x/c)_{\text{tr,optimized}} = 0.160$ on the airfoil section side. As in the baseline case, transition takes place upstream of the shock location for the optimized airfoil. In cases

for which transition is triggered by the adverse pressure gradient in the shock wave region, unsteady separation may occur, leading to potential difficulties in the convergence process [31]. On the airfoil pressure side, the optimizer delays transition from $(x/c)_{\text{tr,baseline}} = 0.39$ to $(x/c)_{\text{tr,optimized}} = 0.47$. Skin friction coefficient distributions for the baseline and transitional ASO cases are shown in Fig. 11.

In transonic airfoils, it is important to consider the total drag as the objective function. In this flight regime, the pressure drag becomes relevant due to the presence of the shock wave [45]. This is motivated by the fact that the optimizer should be able to balance between laminar flow region extension and shock wave strength reduction. The fully-turbulent and transitional ASO cases result in a shock wave strength reduction on the airfoil suction side. In the fully-turbulent ASO, the optimizer weakens the shock to reduce total drag. This same trend was observed in the work of He et al. [71]. When a fully-turbulent flow regime is assumed, a sequence of weak shocks is observed from $(x/c) = 0.4$ to $(x/c) = 0.5$ in the optimized airfoil. These low intensity shocks were also reported by Chen and Fidkowski [89]. In the transitional ASO, the shock wave, although weakened when compared to the baseline design, is stronger than in its fully-turbulent ASO counterpart airfoil. In the transitional ASO, the optimizer compromises between laminar flow extension and shock wave intensity and results in an extension of the laminar flow region combined to a shock that is weaker than the one seen in the baseline design. The pressure coefficient distributions for the baseline and transitional ASO cases are shown in Fig. 11 and indicate that the optimizer indeed reduces the shock wave strength in both fully-turbulent and transitional optimizations.

Skin friction and pressure coefficient distributions for the natural laminar flow airfoil in fully-turbulent mode are also seen in Fig. 11. When laminar flow is lost, the transitional optimized airfoil experiences an increased skin friction coefficient distribution, specially close to the leading edge. In this scenario, the pressure coefficient is similar to the transitional one, except for the region where the shock wave effects are observed. With a fully turbulent boundary layer, the shock wave strength is reduced when compared to the transitional case. The shock wave is also located upstream of its corresponding counterpart in the transitional optimized airfoil with transition included. These observations highlight the impact of transition prediction on the shock wave computation and its interaction with the boundary layer.

The pressure contours for both fully-turbulent and transitional optimized airfoils further confirm the shock wave intensity reduction achieved during the optimization. The pressure field is normalized by the freestream value. The pressure contours for baseline and optimized airfoils for both fully-turbulent and transitional cases are shown in Fig. 12.

4.3 Transitional ASO Convergence History

When performing ASO simulations, it is helpful to observe how the optimization evolves. To do this, we analyze the optimality and feasibility histories, which quantify the satisfaction of the first-order KKT conditions and constraint violation, respectively [79]. The merit function quantifies the objective progress throughout the optimization iterations.

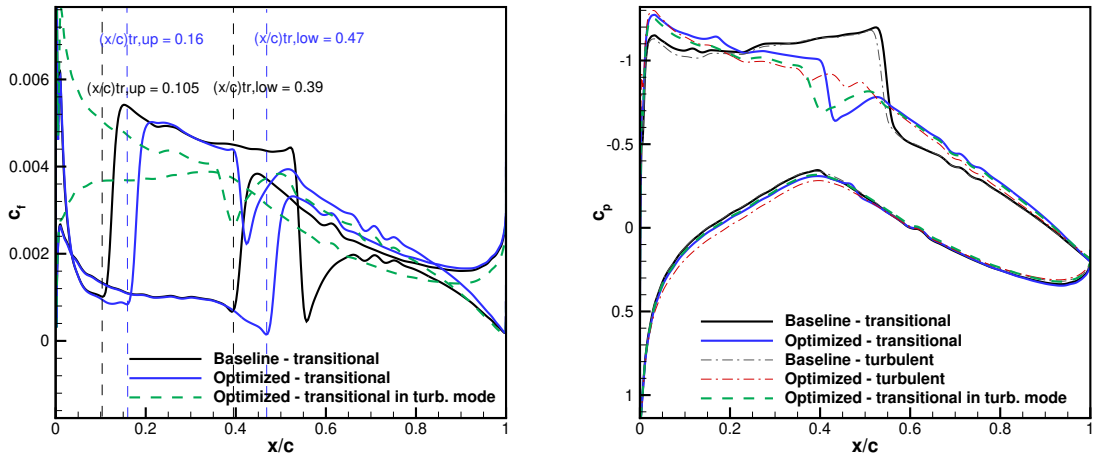

(a) c_f (b) c_p

Figure 11: Skin friction (left) and pressure (right) coefficients for the transitional ASO.

For the transitional NACA 0012 multipoint ASO introduced in Sec. 4.1, the major optimality and feasibility metrics converge to a tolerance of 10^{-4}. These tolerances are achieved after 14 major iterations, as shown in Fig. 13. The merit function is also displayed in Fig. 13. For the drag minimization problem in the multipoint ASO, the objective is the average between the drag coefficients at both flight conditions. The results in Fig. 13 show an initial steep decrease in the merit function, followed by a plateau towards the end of the optimization process. The optimality reaches 8.4×10^{-5}, while the feasibility is 4.3×10^{-6} for the last iteration. For this optimization problem, SNOPT estimates that a variation in the fourth significant digit could be reached if the optimization were able to progress further. This means that improvements of the order of a hundredth of a drag count could be expected, which indicates that the results are converged from an engineering perspective.

For the transonic transitional ASO based on the RAE 2822 airfoil presented in Sec. 4.2, the optimality initially increases, and then decreases toward the end of the optimization process. The feasibility first experiences an increase, and then decreases to eventually reach a plateau. The merit function, which is correlated with the objective, exhibits a continuous decrease, indicating that the optimization process is able to reduce the drag coefficient, as seen in Sec. 4.2. The optimization history results for the RAE 2822 airfoil can be seen in Fig. 14. For this transitional ASO, the optimizer reduces the drag by 30.5 drag counts. If more accurate gradients were available and the optimization were able to progress further, SNOPT estimates that a drag coefficient improvement of the order of 1 drag count could be expected. This is about 3% relative to the drag coefficient reduction already achieved.

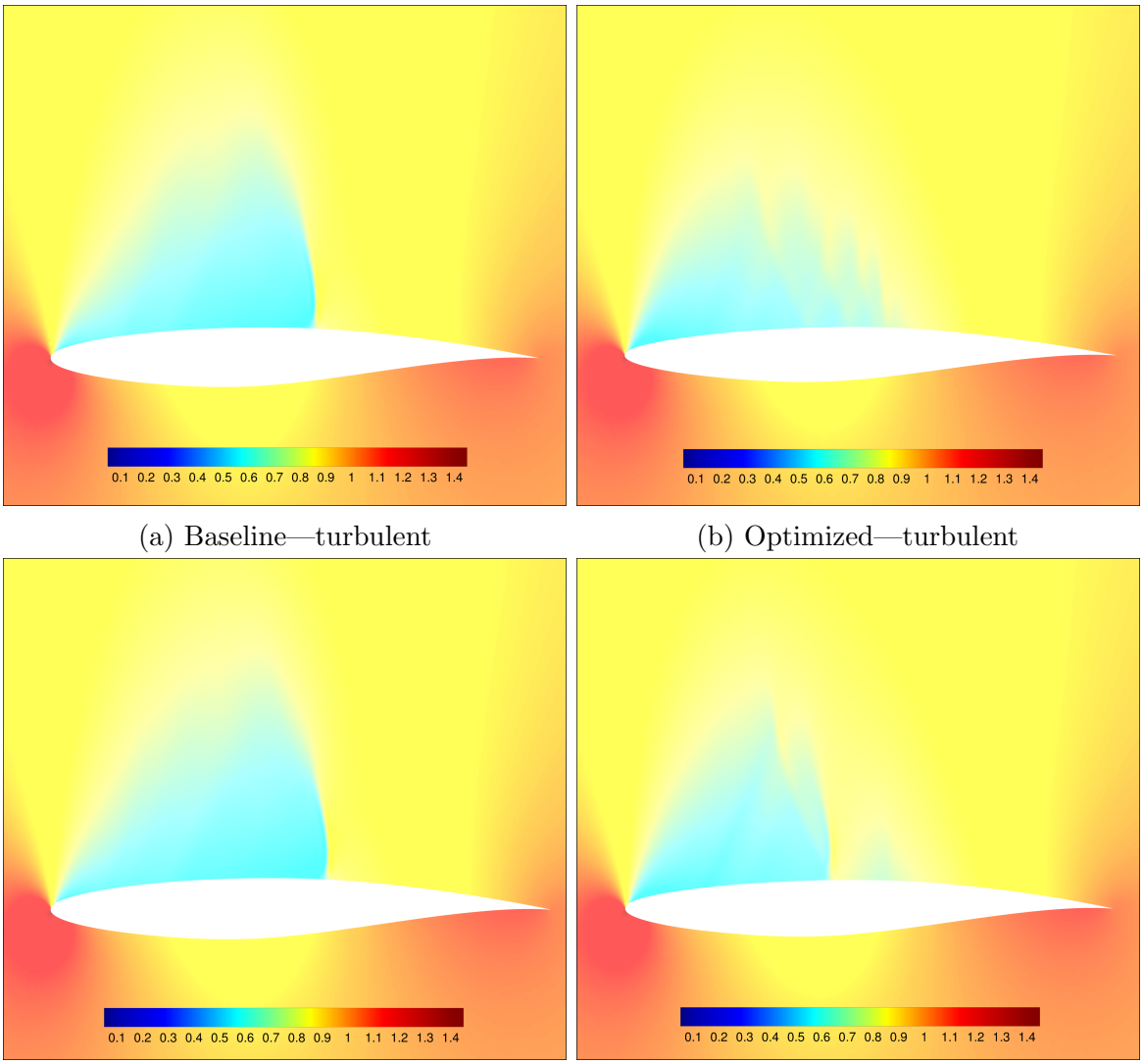

(a) Baseline—turbulent

(b) Optimized—turbulent

(c) Baseline—transitional

(d) Optimized—transitional

Figure 12: Pressure contours for baseline and optimized airfoils in fully-turbulent and transitional modes.

5 Conclusions

Reynolds-Averaged Navier–Stokes (RANS) models, which are currently used to account for turbulence effects in the majority of CFD simulations across the industry, assume a fully-turbulent flow field. By doing so, any information on the laminar and transitional flows that precede the fully-turbulent state is lost in the modeling process. This drawback results from the Favre averaging procedure used to derive the RANS equations, which filters out all flow stability modes that, once amplified, may trigger transition to turbulence.

In this work, we presented aerodynamic shape optimization (ASO) results that do include transition to turbulence. Transition to turbulence effects were included in the CFD simulations by using the AFT-S model. These results considered airfoil flows

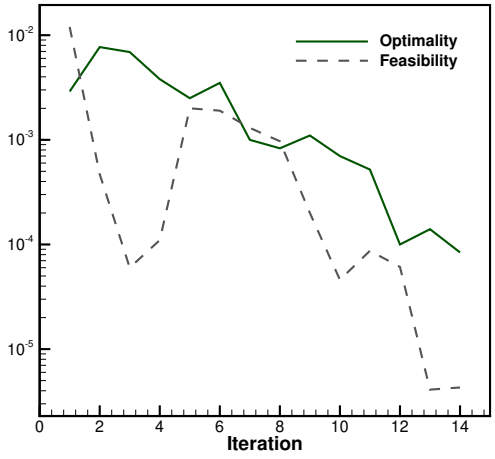

(a) Optimality and feasibility

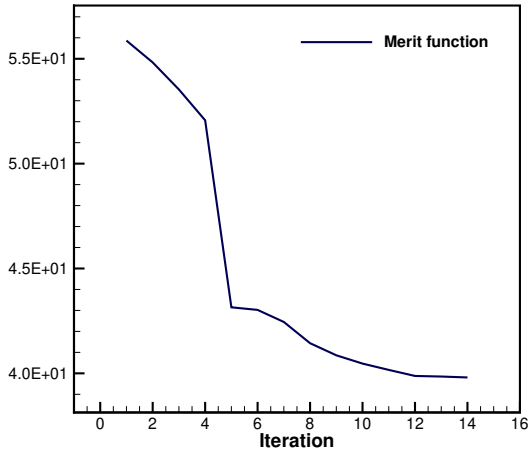

(b) Merit function

Figure 13: Optimality, feasibility (left), and merit function (right) for the transitional multipoint ASO of the NACA 0012 case.

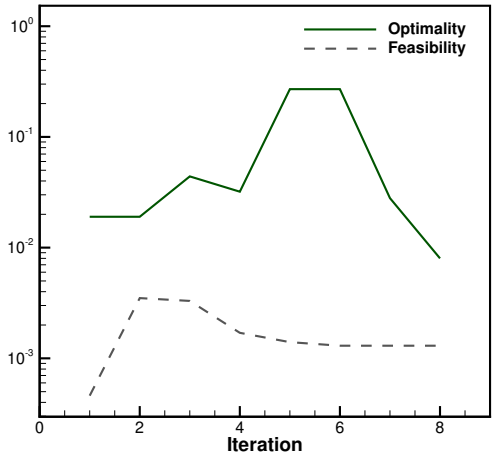

(a) Optimality and feasibility

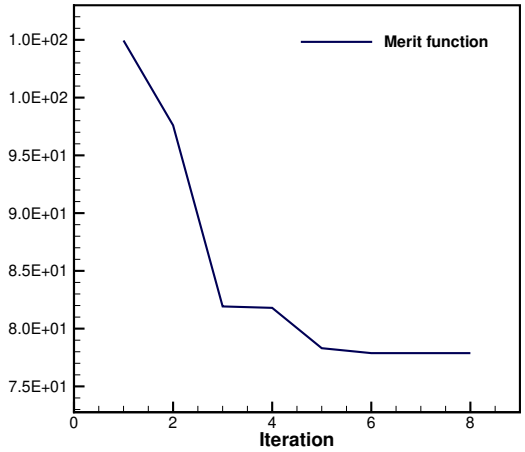

(b) Merit function

Figure 14: Optimality, feasibility (left), and merit function (right) for the transitional ASO of the RAE 2822 transonic case.

from the lower subsonic to the transonic flow regimes and represent a CFD-based ASO framework able to explore laminar flow technologies with a modeling strategy that is compatible with industry requirements. In the subsonic flow regime, drag minimization is achieved through an extension of the laminar flow region. For airfoils in this type of flow, drag is dominated by skin friction effects, and this is why the optimization process seeks to increase the laminar flow extent.

In transonic cases, the drag minimization corresponds to a balance between increasing the laminar flow extent and weakening the shock wave. Compared to fully-

turbulent optimization cases for airfoils in transonic flow, the design resulting from the transitional ASO exhibits a stronger shock wave. Still, it results in a considerably smaller total drag coefficient. For the transonic test case explored in this thesis, the transition to turbulence occurs upstream of the shock wave in the airfoil suction side, and the pressure side is shock-free. We also considered simulations with natural laminar flow airfoils in fully-turbulent mode, as caused by surface contamination, which triggers early transition to turbulence. For these cases, which represent a worse case scenario, the resulting drag coefficients are comparable to the ones obtained in the designs resulting from the fully-turbulent ASO simulations.

The ASO framework including transition effects proposed in this paper makes possible the design of efficient, low drag airplanes that benefit from extended laminar flow regions. By using the AFT-S model, no external modules to the CFD solver are needed to compute transition to turbulence effects. This leads to a high-fidelity, adjoint-based ASO tool that is compatible with industry standards.

Acknowledgments

The authors gratefully acknowledge the support provided by Conselho Nacional de Desenvolvimento Científico e Tecnológico, CNPq, Brazil, under Research Grant No. 205552/2014-5. The first author thanks Dr. Ping He, Dr. Charles Mader, and Dr. Eirikur Jonsson for the insightful discussions on adjoint methods and optimization. This work used the Extreme Science and Engineering Discovery Environment (XSEDE), which is supported by The National Science Foundation grant number ACI-1548562.

References

References

[1] Schrauf, G., "Key Aerodynamic Technologies for Aircraft Performance Improvement," Presented at the Fifth Community Aeronautical Days, June 2006.

[2] Halila, G. L. O., Bigarella, E. D. V., and Azevedo, J. L. F., "Numerical Study on Transitional Flows Using a Correlation-Based Transition Model," *Journal of Aircraft*, Vol. 53, No. 4, 2016, pp. 922–941. doi:10.2514/1.C033311.

[3] Halila, G. L. O., Bigarella, E. D. V., Antunes, A. P., and Azevedo, J. L. F., "An Efficient Setup for Freestream Turbulence on Transition Prediction over Aerospace Configurations," *Aerospace Science and Technology*, Vol. 81, 2018, pp. 259–271. doi:10.1016/j.ast.2018.08.013.

[4] Halila, G. L. O., Antunes, A. P., Silva, R. G., and Azevedo, J. L. F., "Effects of Boundary Layer Transition on the Aerodynamic Analysis of High-lift Systems," *Aerospace Science and Technology*, Vol. 90, 2019, pp. 233–245. doi:10.1016/j.ast.2019.04.051.

[5] van Dam, C. P., "The Aerodynamic Design of Multi-Element High-Lift Systems for Transport Airplanes," *Progress in Aerospace Sciences*, Vol. 38, No. 2, 2002, pp. 101–144. doi:10.1016/S0376-0421(02)00002-7.

[6] van Dam, C. P., Los, S. M., Miley, S., Roback, V. E., Yip, L. P., Bertelrud, A., and Vijgen, P. M. H. W., "In-Flight Boundary-Layer Measurements on a High-Lift System: Main Element and Flap," *Journal of Aircraft*, Vol. 34, No. 6, 1997, pp. 757–763. doi:10.2514/2.2253.

[7] Eliasson, P., Peng, S. H., and Hanifi, A., "Improving the Prediction for the NASA High-Lift Trap Wing Model," AIAA Paper No. 2011-0867*, Proceedings of the 49th AIAA Aerospace Sciences Meeting Including the New Horizons Forum and Aerospace Exposition*, Orlando, FL, 2011. doi:10.2514/6.2011-867.

[8] Eliasson, P., Hanifi, A., and Peng, S. H., "Influence of Transition on High-Lift Prediction for the NASA Trap Wing Model," AIAA Paper No. 2011-3009*, Proceedings of the 29th AIAA Applied Aerodynamics Conference*, Honolulu, HI, 2011. doi:10.2514/6.2011-3009.

[9] Langtry, R. B., and Menter, F. R., "Correlation-Based Transition Modeling for Unstructured Parallelized Computational Fluid Dynamics Codes," *AIAA Journal*, Vol. 47, No. 12, 2009, pp. 2894–2906. doi:10.2514/1.42362.

[10] Menter, F. R., Esch, T., S., and Kubacki, "Transition Modeling Based on Local Variables," *5th International Symposium on Turbulence Modeling and Measurements*, Spain, 2002.

[11] Menter, F. R., Langtry, R. B., Likki, S. R., Suzen, Y. B., Huang, P., and Volker, S., "A Correlation Based Transition Model Using Local Variables. Part 1: Model Formulation," *ASME TURBO EXPO 2004*, Vienna, Austria, 2004.

[12] Langtry, R. B., Menter, F. R., Likki, S. R., Suzen, Y. B., Huang, P., and Volker, S., "A Correlation Based Transition Model Using Local Variables. Part 2: Test Cases and Industrial Applications," *ASME TURBO EXPO 2004*, Vienna, Austria, 2004.

[13] Menter, F. R., "Two-equation eddy-viscosity turbulence models for engineering applications," *AIAA Journal*, Vol. 32, No. 8, 1994, pp. 1598–1605. doi:10.2514/3.12149.

[14] Coder, J. G., and Maughmer, M. D., "Computational Fluid Dynamics Compatible Transition Modeling Using an Amplification Factor Transport Equation," *AIAA Journal*, Vol. 52, No. 11, 2014, pp. 2506–2512. doi:10.2514/1.J052905.

[15] Drela, M., and Giles, M. B., "Viscous-Inviscid Analysis of Transonic and Low Reynolds Number Airfoils," *Journal of Aircraft*, Vol. 25, No. 10, 1987, pp. 1347–1355. doi:10.2514/6.1986-1786.

[16] Spalart, P., and Allmaras, S., "A One-Equation Turbulence Model for Aerodynamic Flows," *30th Aerospace Sciences Meeting and Exhibit*, 1992. doi:10.2514/6.1992-439.

[17] Coder, J. G., "Further Development of the Amplification Factor Transport Transition Model for Aerodynamic Flows," *Proceedings of the AIAA Scitech 2019 Forum*, San Diego, CA., 2019. doi:10.2514/6.2019-0039.

[18] Lyu, Z., Kenway, G. K. W., and Martins, J. R. R. A., "Aerodynamic Shape Optimization Investigations of the Common Research Model Wing Benchmark," *AIAA Journal*, Vol. 53, No. 4, 2015, pp. 968–985. doi:10.2514/1.J053318.

[19] Chen, S., Lyu, Z., Kenway, G. K. W., and Martins, J. R. R. A., "Aerodynamic Shape Optimization of the Common Research Model Wing-Body-Tail Configuration," *Journal of Aircraft*, Vol. 53, No. 1, 2016, pp. 276–293. doi:10.2514/1.C033328.

[20] Kenway, G. K. W., and Martins, J. R. R. A., "Multipoint High-Fidelity Aerostructural Optimization of a Transport Aircraft Configuration," *Journal of Aircraft*, Vol. 51, No. 1, 2014, pp. 144–160. doi:10.2514/1.C032150.

[21] Gray, J. S., and Martins, J. R. R. A., "Coupled Aeropropulsive Design Optimization of a Boundary-Layer Ingestion Propulsor," *The Aeronautical Journal*, Vol. 123, No. 1259, 2019, pp. 121–137. doi:10.1017/aer.2018.120.

[22] Lions, J. L., *Optimal Control of Systems Governed by Partial Differential Equations*, Springer–Verlag, New York, 1971.

[23] Bryson, A. E., and Ho, Y.-C., *Applied Optimal Control: Optimization, Estimation, and Control*, John Wiley & Sons, 1975.

[24] Haug, E. J., and Arora, J. S., "Optimal Mechanical Design Techniques Based on Optimal Control Methods," *Proceedings of the 1st ASME Design Technology Transfer Conference*, New York, NY, 1974, pp. 65–74.

[25] Arora, J. S., and Haug, E. J., "Efficient Optimal Design of Structures by Generalized Steepest Descent Programming," *International Journal for Numerical Methods in Engineering*, Vol. 10, 1976, pp. 747–766. doi:10.1002/nme.1620100404.

[26] Pironneau, O., "On Optimum Profiles in Stokes Flow," *Journal of Fluid Mechanics*, Vol. 59, No. 01, 1973, pp. 117–128. doi:10.1017/S002211207300145X.

[27] Pironneau, O., "On optimum design in fluid mechanics," *Journal of Fluid Mechanics*, Vol. 64, No. 01, 1974, pp. 97–110. doi:10.1017/S0022112074002023.

[28] Jameson, A., "Aerodynamic Design via Control Theory," *Journal of Scientific Computing*, Vol. 3, No. 3, 1988, pp. 233–260. doi:10.1007/BF01061285.

[29] Jameson, A., Martinelli, L., and Pierce, N. A., "Optimum Aerodynamic Design Using the Navier–Stokes Equations," *Theoretical and Computational Fluid Dynamics*, Vol. 10, No. 1–4, 1998, pp. 213–237. doi:10.1007/s001620050060.

[30] Nielsen, E. J., and Anderson, W. K., "Aerodynamic Design Optimization on Unstructured Meshes Using the Navier–Stokes Equations," *AIAA Journal*, Vol. 37, No. 11, 1999, pp. 1411–1419. doi:10.2514/2.640.

[31] Rashad, R., and Zingg, D. W., "Aerodynamic Shape Optimization for Natural Laminar Flow Using a Discrete-Adjoint Approach," *AIAA Journal*, Vol. 54, No. 11, 2016, pp. 3321–3337. doi:10.2514/1.J054940.

[32] Dodbele, S. S., "Design Optimization of Natural Laminar Flow Bodies in Compressible Flow," *Journal of Aircraft*, Vol. 29, No. 3, 1992, pp. 343–347. doi:10.2514/3.46167.

[33] Granville, P. S., "The Calculation of the Viscous Drag of Bodies of Revolution," David taylor model basin rept. 849, NAVY Department, Washington, D.C., July 1953.

[34] Green, B., Whitesides, J., Campbell, R., and Mineck, R., "A Method for the Constrained Design of Natural Laminar Flow Airfoils," *Proceedings of the 14th Applied Aerodynamics Conference*, AIAA, New Orleans, LA, 1996. doi:10.2514/6.1996-2502.

[35] Kroo, I., and Sturdza, P., "Laminar Flow Control—A Systems Approach," *Proceedings of the 41st Aerospace Sciences Meeting and Exhibit*, AIAA, Reno, NV, 2003. doi:10.2514/6.2003-774.

[36] Amoignon, O. G., Pralits, J. O., Hanifi, A., Berggren, M., and Henningson, D. S., "Shape optimization for delay of laminar-turbulent transition," *AIAA journal*, Vol. 44, No. 5, 2006, pp. 1009–1024. doi:10.2514/1.12431.

[37] Driver, J., and Zingg, D. W., "Numerical Aerodynamic Optimization Incorporating Laminar-Turbulent Transition Prediction," *AIAA Journal*, Vol. 45, No. 8, 2007, pp. 1810–1818. doi:10.2514/1.23569.

[38] Drela, M., *A User's Guide to MSES 3.05*, MIT Department of Aeronautics and Astronautics, http://web.mit.edu/drela/Public/web/mses/mses.pdf, July 2007.

[39] Lee, J.-D., and Jameson, A., "Natural-Laminar-Flow Airfoil and Wing Design by Adjoint Method and Automatic Transition Prediction," *47th AIAA Aerospace Sciences Meeting including The New Horizons Forum and Aerospace Exposition*, 2009. doi:10.2514/6.2009-897.

[40] Lee, J.-D., and Jameson, A., "NLF Wing Design by Adjoint Method and Automatic Transition Prediction," Ph.D. thesis, Stanford University, Stanford, CA, USA, 2009.

[41] Baldwin, B., and Lomax, H., "Thin-Layer Approximation and Algebraic Model for Separated Turbulent Flows," *Proceedings of the 16th AIAA Aerospace Sciences Meeting*, AIAA, Huntsville, AL, 1978. doi:10.2514/6.1978-257.

[42] Khayatzadeh, P., and Nadarajah, S. K., "Aerodynamic Shape Optimization via Discrete Viscous Adjoint Equations for the k-ω SST Turbulence and γ - Re_θ Transition Models," *Proceedings of the 49th AIAA Aerospace Sciences Meeting including the New Horizons Forum and Aerospace Exposition*, Orlando,FL, 2011. doi:10.2514/6.2011-1247.

[43] Khayatzadeh, P., and Nadarajah, S., "Aerodynamic Shape Optimization of Natural Laminar Flow (NLF) airfoils," *50th AIAA Aerospace Sciences Meeting including the New Horizons Forum and Aerospace Exposition*, 2012, pp. 1–15. doi:10.2514/6.2012-61.

[44] Li, J., Gao, Z., Huang, J., and Zhao, K., "Robust design of NLF airfoils," *Chinese Journal of Aeronautics*, Vol. 26, No. 2, 2013, pp. 309–318. doi:10.1016/j.cja.2013.02.007.

[45] Zhao, K., Gao, Z.-h., and Huang, J.-t., "Robust Design of Natural Laminar Flow Supercritical Airfoil by Multi-Objective Evolution Method," *Applied Mathematics and Mechanics*, Vol. 35, No. 2, 2014, pp. 191–202. doi:10.1007/s10483-014-1783-6.

[46] Robitaille, M., Mosahebi, A., and Éric Laurendeau, "Design of adaptive transonic laminar airfoils using the γ - Re_θ transition model," *Aerospace Science and Technology*, Vol. 46, 2015, pp. 60 – 71. doi:https://doi.org/10.1016/j.ast.2015.06.027, URL http://www.sciencedirect.com/science/article/pii/S1270963815002047.

[47] Cliquet, J., Houdeville, R., and Arnal, D., "Application of Laminar-Turbulent Transition Criteria in Navier–Stokes Computations," *AIAA Journal*, Vol. 46, No. 5, 2008, pp. 1182–1190. doi:10.2514/1.30215.

[48] Shi, Y., Mader, C. A., He, S., Halila, G. L. O., and Martins, J. R. R. A., "Natural Laminar-Flow Airfoil Optimization Design Using a Discrete Adjoint Approach," *AIAA Journal*, 2020. doi:10.2514/1.J058944.

[49] Coder, J. G., Pulliam, T. H., Hue, D., Kenway, G. K. W., and Sclafani, A. J., "Contributions to the 6th AIAA CFD Drag Prediction Workshop Using Structured Grid Methods," *AIAA SciTech Forum*, American Institute of Aeronautics and Astronautics, 2017. doi:10.2514/6.2017-0960.

[50] Coder, J. G., Pulliam, T. H., and Jensen, J. C., "Contributions to HiLIftPW-3 Using Structured, Overset Grid Methods," *Proceedings of the AIAA Aerospace Sciences Meeting, AIAA SciTech Forum*, Kissimmee, FL, 2018. doi:10.2514/6.2018-1039.

[51] Carnes, J. A., and Coder, J. G., "Effect of Crossflow on the S-76 and PSP Rotors in Hover," *Proceedings of the AIAA Scitech 2020 Forum*, Orlando, FL., 2020. doi:10.2514/6.2020-0773.

[52] Langtry, R., "Extending the Gamma-Rethetat Correlation Based Transition Model for Crossflow Effects (Invited)," 2015, pp. 1–12. doi:10.2514/6.2015-2474.

[53] Shi, Y., Gross, R., Mader, C. A., and Martins, J. R. R. A., "Transition Prediction Based on Linear Stability Theory with the RANS Solver for Three-Dimensional Configurations," *Proceedings of the AIAA Aerospace Sciences Meeting, AIAA SciTech Forum*, Kissimmee, FL, 2018. doi:10.2514/6.2018-0819.

[54] Halila, G. L. O., Chen, G., Shi, Y., Fidkowski, K. J., Martins, J. R. R. A., and de Mendonça, M. T., "High-Reynolds Number Transitional Flow Simulation via Parabolized Stability Equations with an Adaptive RANS Solver," *Aerospace Science and Technology*, Vol. 91, 2019, pp. 321–336. doi:10.1016/j.ast.2019.05.018.

[55] Mack, L. M., "Transition Prediction and Linear Stability Theory," AGARD Report CP224, 1977.

[56] Allmaras, S. R., Johnson, F. T., and Spalart, P. R., "Modifications and Clarifications for the Implementation of the Spalart-Allmaras Turbulence Model," Big Island, Hawaii, 2012. URL `http://www.iccfd.org/iccfd7/assets/pdf/papers/ICCFD7-1902_paper.pdf`.

[57] Halila, G., Yildirim, A., Mader, C. A., Fidkowski, K. J., and Martins, J. R. R. A., "RANS-based Transition to Turbulence Prediction in an Approximate Newton–Krylov Solver," *International Journal for Numerical Methods in Fluids*, 2020. (Submitted).

[58] Kreisselmeier, G., and Steinhauser, R., "Systematic Control Design by Optimizing a Vector Performance Index," *International Federation of Active Controls Symposium on Computer-Aided Design of Control Systems, Zurich, Switzerland*, 1979. doi:10.1016/S1474-6670(17)65584-8.

[59] Poon, N. M. K., and Martins, J. R. R. A., "An Adaptive Approach to Constraint Aggregation Using Adjoint Sensitivity Analysis," *Structural and Multidisciplinary Optimization*, Vol. 34, No. 1, 2007, pp. 61–73. doi:10.1007/s00158-006-0061-7.

[60] Lambe, A. B., Martins, J. R. R. A., and Kennedy, G. J., "An Evaluation of Constraint Aggregation Strategies for Wing Box Mass Minimization," *Structural and Multidisciplinary Optimization*, Vol. 55, No. 1, 2017, pp. 257–277. doi:10.1007/s00158-016-1495-1.

[61] Mader, C. A., Kenway, G. K. W., Yildirim, A., and Martins, J. R. R. A., "ADflow—An open-source computational fluid dynamics solver for aerodynamic and multidisciplinary optimization," *Journal of Aerospace Information Systems*, 2020. doi:10.2514/1.I010796.

[62] Jameson, A., Schmidt, W., and Turkel, E., "Numerical Solution of the Euler Equations by Finite Volume Methods Using Runge–Kutta Time Stepping Schemes," *14th Fluid and Plasma Dynamics Conference*, 1981. doi:10.2514/6.1981-1259.

[63] Turkel, E., and Vatsa, V. N., "Effects of Artificial Viscosity on Three-Dimensional Flow Solutions," *AIAA Journal*, Vol. 32, 1994, pp. 39–45. doi:10.2514/3.11948.

[64] van Leer, B., "Towards the ultimate conservative difference scheme. V. A second-order sequel to Godunov's method," *Journal of Computational Physics*, Vol. 32, 1979, pp. 101–136. doi:10.1016/0021-9991(79)90145-1.

[65] Roe, P. L., "Approximate Riemann Solvers, Parameter Vectors, and Difference Schemes," *Journal of Computational Physics*, Vol. 43, 1981, pp. 357–372. doi:10.1016/0021-9991(81)90128-5.

[66] Klopfer, G., Hung, C., Van der Wijngaart, R., and Onufer, J., "A diagonalized diagonal dominant alternating direction implicit (D3ADI) scheme and subiteration correction," *29th AIAA, Fluid Dynamics Conference, Albuquerque, NM*, 1998. doi:10.2514/6.1998-2824.

[67] Yildirim, A., Kenway, G. K. W., Mader, C. A., and Martins, J. R. R. A., "A Jacobian-free approximate Newton–Krylov startup strategy for RANS simulations," *Journal of Computational Physics*, Vol. 397, 2019, p. 108741. doi:10.1016/j.jcp.2019.06.018.

[68] Kenway, G. K. W., Mader, C. A., He, P., and Martins, J. R. R. A., "Effective Adjoint Approaches for Computational Fluid Dynamics," *Progress in Aerospace Sciences*, Vol. 110, 2019, p. 100542. doi:10.1016/j.paerosci.2019.05.002.

[69] Kenway, G. K. W., and Martins, J. R. R. A., "Buffet Onset Constraint Formulation for Aerodynamic Shape Optimization," *AIAA Journal*, Vol. 55, No. 6, 2017, pp. 1930–1947. doi:10.2514/1.J055172.

[70] Bons, N. P., He, X., Mader, C. A., and Martins, J. R. R. A., "Multimodality in Aerodynamic Wing Design Optimization," *AIAA Journal*, Vol. 57, No. 3, 2019, pp. 1004–1018. doi:10.2514/1.J057294.

[71] He, X., Li, J., Mader, C. A., Yildirim, A., and Martins, J. R. R. A., "Robust aerodynamic shape optimization—from a circle to an airfoil," *Aerospace Science and Technology*, Vol. 87, 2019, pp. 48–61. doi:10.1016/j.ast.2019.01.051.

[72] Mangano, M., and Martins, J. R. R. A., "Multipoint Aerodynamic Shape Optimization for Subsonic and Supersonic Regimes," *Journal of Aircraft*, 2020. doi:10.2514/1.C035826.

[73] Kenway, G. K., Kennedy, G. J., and Martins, J. R. R. A., "A CAD-Free Approach to High-Fidelity Aerostructural Optimization," *Proceedings of the 13th AIAA/ISSMO Multidisciplinary Analysis Optimization Conference*, Fort Worth, TX, 2010. doi:10.2514/6.2010-9231.

[74] Secco, N. R., Kenway, G. K. W., He, P., Mader, C. A., and Martins, J. R. R. A., "Efficient Mesh Generation and Deformation for Aerodynamic Shape Optimization," *AIAA Journal*, 2020. (Submitted).

[75] Sederberg, T. W., and Parry, S. R., "Free-form Deformation of Solid Geometric Models," *SIGGRAPH Comput. Graph.*, Vol. 20, No. 4, 1986, pp. 151–160. doi:10.1145/15886.15903.

[76] Luke, E., Collins, E., and Blades, E., "A Fast Mesh Deformation Method Using Explicit Interpolation," *Journal of Computational Physics*, Vol. 231, No. 2, 2012, pp. 586–601. doi:10.1016/j.jcp.2011.09.021.

[77] Nielsen, E. J., and Park, M. A., "Using an adjoint approach to eliminate mesh sensitivities in computational design," *AIAA journal*, Vol. 44, No. 5, 2006, pp. 948–953. doi:10.2514/1.16052.

[78] Widhalm, M., Brezillon, J., Ilic, C., and Leicht, T., "Investigation on Adjoint Based Gradient Computations for Realistic 3D Aero-Optimization," *13th AIAA/ISSMO Multidisciplinary Analysis and Optimization Conference*, Fort Worth, TX, 2010, pp. 1–17. doi:10.2514/6.2010-9129.

[79] Gill, P. E., Murray, W., and Saunders, M. A., "SNOPT: An SQP Algorithm for Large-Scale Constrained Optimization," *SIAM Review*, Vol. 47, No. 1, 2005, pp. 99–131. doi:10.1137/S0036144504446096.

[80] Perez, R. E., Jansen, P. W., and Martins, J. R. R. A., "pyOpt: A Python-Based Object-Oriented Framework for Nonlinear Constrained Optimization," *Structural and Multidisciplinary Optimization*, Vol. 45, No. 1, 2012, pp. 101–118. doi:10.1007/s00158-011-0666-3.

[81] Lyu, Z., and Martins, J. R. R. A., "Aerodynamic Design Optimization Studies of a Blended-Wing-Body Aircraft," *Journal of Aircraft*, Vol. 51, No. 5, 2014, pp. 1604–1617. doi:10.2514/1.C032491.

[82] Brooks, T. R., Kenway, G. K. W., and Martins, J. R. R. A., "Benchmark Aerostructural Models for the Study of Transonic Aircraft Wings," *AIAA Journal*, Vol. 56, No. 7, 2018, pp. 2840–2855. doi:10.2514/1.J056603.

[83] He, P., Mader, C. A., Martins, J. R. R. A., and Maki, K. J., "An Aerodynamic Design Optimization Framework Using a Discrete Adjoint Approach with OpenFOAM," *Computers & Fluids*, Vol. 168, 2018, pp. 285–303. doi:10.1016/j.compfluid.2018.04.012.

[84] Madsen, M. H. A., Zahle, F., Sørensen, N. N., and Martins, J. R. R. A., "Multipoint high-fidelity CFD-based aerodynamic shape optimization of a 10 MW wind turbine," *Wind Energy Science*, Vol. 4, 2019, pp. 163–192. doi:10.5194/wes-4-163-2019.

[85] He, P., Mader, C. A., Martins, J. R. R. A., and Maki, K. J., "DAFoam: An Open-Source Adjoint Framework for Multidisciplinary Design Optimization with OpenFOAM," *AIAA Journal*, Vol. 58, No. 3, 2020. doi:10.2514/1.J058853.

[86] Martins, J. R. R. A., "Perspectives on Aerodynamic Design Optimization," *AIAA SciTech Forum*, AIAA, Orlando, FL, 2020. doi:10.2514/6.2020-0043.

[87] Abbott, I. H., and Von Doenhoff, A. E., *Theory of wing sections, including a summary of airfoil data*, Dover Publications, New York, 1959.

[88] Jones, R. T., *Wing Theory*, Princeton University Press, Princeton, New Jersey, 1990.

[89] Chen, G., and Fidkowski, K. J., "Discretization Error Control for Constrained Aerodynamic Shape Optimization," *Journal of Computational Physics*, Vol. 387, 2019, pp. 163–185. doi:https://doi.org/10.1016/j.jcp.2019.02.038, URL http://www.sciencedirect.com/science/article/pii/S002199911930155X.